

## Article

# Dynamic Characteristics of Transverse-Magnetic-Field Induced Arc for Plasma-Jet-Triggered Protective Gas Switch in Hybrid UHVDC System

Wen Wang <sup>1,\*</sup> , Zhibing Li <sup>1</sup>, Keli Gao <sup>1</sup>, Enyuan Dong <sup>2</sup>, Xuebin Qu <sup>2</sup> and Xiaodong Xu <sup>1</sup><sup>1</sup> High Voltage Department, China Electric Power Research Institute, Beijing 100192, China<sup>2</sup> School of Electrical Engineering, Dalian University of Technology, Dalian 116024, China

\* Correspondence: wangwen@epri.sgcc.com.cn

**Abstract:** A plasma jet-triggered gas switch (PJT-GS) has been developed as an important piece of equipment to operate in an  $\pm 800$  kV ultra-high voltage direct current transmission system (UHV DC) to achieve grid system protection and control. The crucial factors that would affect its operational performance, such as the current level the PJT-GS could withstand and the gas gap distance between the two rotating electrodes, are comparatively studied in the present work by analysing the arc dynamic characteristics. The rotating electrode used in the PJT-GS is designed with a helical-slotted structure, and the arc can be rotated circularly driven by the produced transverse magnetic field (TMF) along the electrode edge. The objective of such research is to provide a thorough study of the arc dynamic behaviour during the current flowing process of the PJT-GS and also to characterise the physical mechanism that affects the arc rotation and the PJT-GS operation performance. The magnetohydrodynamic-based (MHD) approach is applied by establishing a 3D arc model. Following such a study, the variation of arc characteristics under different operation conditions could be thoroughly determined and it also could provide the guidance for the PJT-GS optimum design reasonably to support its corresponding engineering applications.

**Keywords:** plasma jet-triggered gas switch (PJT-GS); UHVDC; magnetohydrodynamic-based (MHD); arc dynamic characteristics



**Citation:** Wang, W.; Li, Z.; Gao, K.; Dong, E.; Qu, X.; Xu, X. Dynamic Characteristics of Transverse-Magnetic-Field Induced Arc for Plasma-Jet-Triggered Protective Gas Switch in Hybrid UHVDC System. *Energies* **2022**, *15*, 5871. <https://doi.org/10.3390/en15165871>

Academic Editors: Xinyu Wang, Jingzhi Zhang and Gongming Xin

Received: 9 July 2022

Accepted: 1 August 2022

Published: 13 August 2022

**Publisher's Note:** MDPI stays neutral with regard to jurisdictional claims in published maps and institutional affiliations.



**Copyright:** © 2022 by the authors. Licensee MDPI, Basel, Switzerland. This article is an open access article distributed under the terms and conditions of the Creative Commons Attribution (CC BY) license (<https://creativecommons.org/licenses/by/4.0/>).

## 1. Introduction

The plasma jet-triggered gas switch (PJT-GS) has already been widely used as one of the key components in the pulse power supply system, especially working as a device with the functionality of fast closing to achieve grid system control and protection. Actually, such a switch is also a kind of newly developed high-voltage apparatus, in which the gas gap breakover between the two electrodes is achieved by the generated plasma jet to complete the fast closing within an extremely short time interval, even faster than 1 ms. Such an operation could achieve ultra-high-speed control and protection of the electric power grid system and apparatuses in a timely manner. As a key project of the “West-East Electricity Transmission” strategy, the construction of the  $\pm 800$  kV Baihetan-Jiangsu UHV DC project mainly uses the hybrid HVDC transmission technology and applies a kind of controllable self-recovery dissipation device to limit the overvoltage phenomenon so as to sufficiently protect the safe operation of the grid system, as presented in Figure 1. K1 and K2 are two typical switches. The switch of K2 needs to be closed within 1 ms to bypass the controllable part of the arrester when the overvoltage occurs on the transmission line, and the switch of K1 also needs to be speedily closed within 1 ms to earth the busbar to protect the transmission system when an emergency situation occurs such as the energy of the arrester becomes out of limits. It can be seen that a fast and reliable closing of K1 and K2 is the key requirement for the switch for further protection of the system. It should be mentioned that there are the following three types of switches that could be

used as K1 and K2 for this controllable device: mechanical switch, thyristor and PJT-GS. Related research has shown that the PJT-GS is designed with the ability to operate at a lower working coefficient with a fast response to its breakover and also with sufficient capability to withstand the flowed current after the breakover. The operating performance of the PJT-GS has already been proven to withstand the flowed current with a level up to several tens of kiloamperes [1]. With a thorough consideration of these switches with different operation performances, the PJT-GS is more recommended in the present work to ensure the working behaviour of the gas switches of K1 and K2.

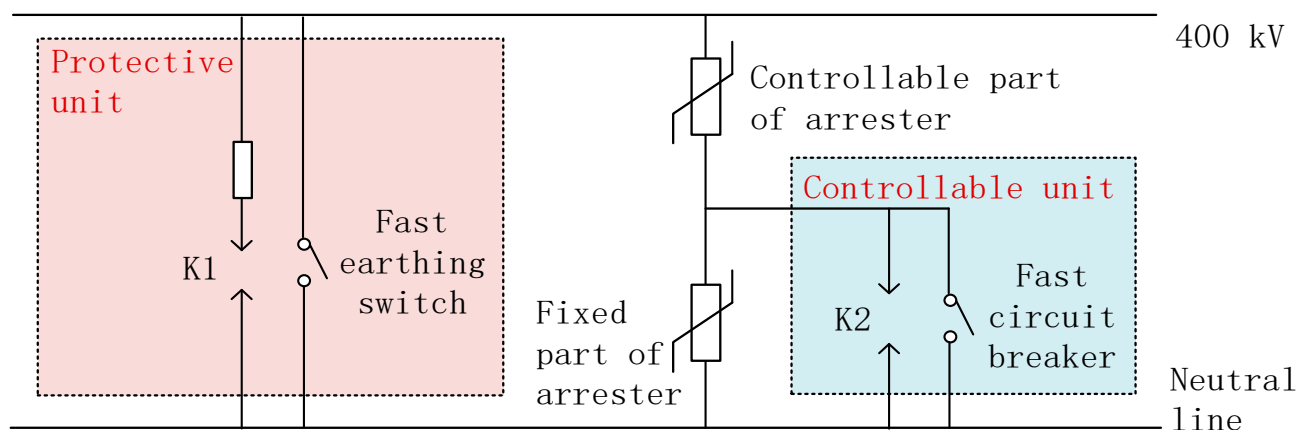


**Figure 1.** Schematic diagram of the controllable self-recovery dissipation device.

Actually, for the structural design of PJT-GS, the core component that would greatly affect its operating performance is the design of the rotary electrode. The pair of electrodes is commonly designed following the concept of that used for the vacuum circuit breaker, which is identified as a kind of magnetic-field-based electrode. An electric arc is formed between the electrodes after the gas gap breakover. The arc is driven by a self-induced magnetic field that is generated by current flowing and such a magnetic field is determined by the corresponding electrodynamic force. Due to the presence of such a force, the arc goes from the electrode center and then travels towards the electrode edge, forcing a circular rotation along the edge with a high velocity during the arcing process. It should be mentioned that the smoothness of the electrode surface has significant effects on the insulation characteristics of the gas gap. Such an electrode design is crucial since it could appropriately control the arc motion to avoid the phenomenon of overheating occurring on the electrode surface and reduce electrode erosion. Besides that, the electric lifetime of the electrode could also be improved.

The control of the rotating arc by the magnetic field is one of the most effective arc controlling technologies. To withstand high current flowing, the electrode is commonly designed with a TMF-based structure, axial magnetic field (AMF)-based structure and hybrid-type electrode that achieves a combination of the impacts of TMF and AMF [2–4]. In the case of TMF arc control, the plate of the electrode is designed with slots so that the self-induced TMF is perpendicular to the arc column. The TMF-based electrode structure has already been widely used for vacuum interrupters, which includes the following three different types: helical-slotted structure, cup-shaped structure and swastika-shaped structure [5]. Investigations of the arc behaviour patterns on the TMF-based electrode for the vacuum circuit breaker have been extensively dealt with by correlating the arc characteristics with the breaker's operating performance and are well described [6–12]. However, there are not many comparative studies so far in the literature in terms of the evaluation of the PJT-GS dynamic performance. It is not only highly related to the structural design of the electrode but also to the operation conditions of the PJT-GS, such as the current level that can be withstood and the gap distance between the two electrodes. The impacts of these two aspects are mutually constrained by each other. The effects of electrode structure design have been thoroughly studied by the authors by proposing an approach that could

quantitatively estimate the arc dynamic behaviour on a spatial scale and also concern the variation of the typical parameters during the arcing process. There is still no evident investigation found that analysed the effects of the PJT-GS operation conditions.

Such a correlation is then detailedly studied in the present work using the computational fluid dynamics (CFD)-based technologies [13–19] to research the performance of PJT-GS systematically. By means of establishing a theoretical arc model that needs to be compared with the experimental results, one of the objectives is to accelerate the optimization design of the PJT-GS. The research strategy of the present work is organised in the following order, first presenting the description of the 3D MHD arc model in the first part of Section 2 and then the experimental setup is described in the second part. In Section 3, the change in the arc rotating behaviour affected by the flowed current level and the gas gap distance are explained in sequence. Conclusions are finally drawn in Section 4.

## 2. 3D Mathematical Arc Model Establishment and Experimental Setup

### 2.1. Establishment of the 3D MHD-Based Mathematical Arc Model

The analysis of the dynamic characteristics of the rotary arc in the present work actually allows the application of the MHD-based approach. The mathematical model is established following the theoretical descriptions of the conservation equations of mass, momentum and energy, in combination with the fundamental equations of electromagnetic fields [20–24]. As the arc plasma is normally generated well above atmospheric pressure, the insulating gas medium is thus assumed to be both in local thermal equilibrium (LTE) and local chemical equilibrium (LCE) states. In addition, quasi-neutrality is also an important property that indicates the negative charges in the plasma are balanced by the positive charges. As is recognized from previous studies, the arc would be deviated from the LTE state within a non-LTE layer very close to the electrode surface due to insufficient collisions and energy transfer between electrons and heavy particles. The thickness of this non-LTE layer is in the order of 0.1 mm [25]. The corresponding non-equilibrium phenomenon in thermal plasma has also been discussed. For example, the non-equilibrium phenomena in (quasi-)thermal plasma flows that can be characterised as kinetic or dissipative are detailedly described by J. P. Trelles [26], C. Mohsni et al. [27] discussed a bidirectional coupling between an LTE argon arc and a refractory cathode involving the non-LTE layer. Important progress has also been achieved in the development and application of the non-equilibrium physical characteristics, especially in thermal plasma models, such as the novel non-equilibrium modelling of a DC electric arc in argon by M. Baeva et al. [28], the arc characterization using two-temperature non-equilibrium plasma flow model by V.G. Bhigamudre et al. [29], and a unified simulation of different modes in DC discharge in nitrogen by A. I. Saifutdinov [30]. In the present work, the aim is to emphatically discuss the diffusion of the electric arc from the macroscopic view to qualitatively understand the arc behaviour in the transient dynamic rotation process. Since the thickness of non-LTE layer is much smaller in comparison with the overall diffusion range of the rotary arc in the PJT-GS chamber, the influence of the non-equilibrium phenomenon on the arc diffusion is thus not included in the work.

The momentum balance considers the terms of pressure gradient and the Lorentz force in the equation, and such an equation could be divided into three equations described by the components of these two terms in the  $x$ ,  $y$ ,  $z$  coordinate system. The energy balance considers the effects of ohmic heating and radiation transfer. A general form for the conservation equations in the Cartesian coordinate could be written as follows [31]:

$$\frac{\partial(\rho\phi)}{\partial t} + \nabla \cdot (\rho\phi\vec{V}) - \nabla \cdot (\Gamma_\phi\nabla\phi) = S_\phi \quad (1)$$

where  $\phi$  is the solved-for variables,  $\rho$  is the density of the insulating gas medium,  $t$  is the time for the transient case,  $\vec{V}$  is the velocity vector,  $\Gamma_\phi$  is the diffusion coefficient and  $S_\phi$  is the source term. This generic form could be disassembled into 6 separate equations,

including one mass conservation equation, three momentum conservation equations in x, y and z directions, one energy conservation equation and the current continuity equation. The corresponding solved-for variables, diffusion coefficients and source terms of these 7 equations are summarized in Table 1. The magnetic flux density  $\vec{B}$  is solved by the current density  $\vec{J}$  and magnetic vector potential  $\vec{A}$  with the following relationship. The symbols for those physical properties in the equations are listed in Table 2.

$$\nabla \times \vec{B} = \nabla \times \nabla \times \vec{A} = \nabla^2 \vec{A} = -\mu_0 \vec{J} \quad (2)$$

**Table 1.** Diffusion coefficients and source terms for the governing equations.

Equation	$\phi$	$\Gamma_\phi$	$S_\phi$
Mass	1	0	0
x-Momentum	$u$	$\mu_l + \mu_t$	$-\frac{\partial P}{\partial x} + J_y B_z - J_z B_y + \text{viscous terms}$
y-Momentum	$v$	$\mu_l + \mu_t$	$-\frac{\partial P}{\partial y} + J_z B_x - J_x B_z + \text{viscous terms}$
z-Momentum	$w$	$\mu_l + \mu_t$	$-\frac{\partial P}{\partial z} + J_x B_y - J_y B_x + \text{viscous terms}$
Energy	$T$	$\lambda_l + \lambda_t$	$\sigma E^2 - q + \frac{dP}{dt} + \text{viscous dissipation}$
Current continuity	$\varphi$	$\sigma$	0

**Table 2.** Explanations of the symbols in the equations.

Symbols	Explanations	Symbols	Explanations
P	Pressure	$\sigma$	Electrical conductivity
T	Temperature	$\lambda_l$	Laminar thermal conductivity
$\mu_l$	Laminar viscosity	$\lambda_t$	Turbulent thermal conductivity
$\mu_t$	Turbulent viscosity	$q$	Net radiation loss per unit volume
$\varphi$	Electric potential	$\mu_0$	Permeability of free space
$\vec{J} (J_x, J_y, J_z)$	Current density	$\vec{A} (A_x, A_y, A_z)$	Magnetic vector potential
$\vec{B} (B_x, B_y, B_z)$	Magnetic flux density	$\vec{E} (E_x, E_y, E_z)$	Electric field

Thermophysical properties are essential in the solution process for studying the arc characteristics, and they are the prerequisite for the numerical simulations of the arc in setting up the physical model. In the present work, the filled insulation gas medium is an SF<sub>6</sub>/N<sub>2</sub> mixture with an absolute pressure of 0.30 MPa at an initial temperature of 300 K. The thermodynamic properties and transport coefficients of the gas mixture are tabulated using the data available from publications [32]. The local properties of the gas mixture during the iteration process are obtained by interpolation.

The software of Ansys Fluent is applied with an improving development of the arc model using user-defined functions (UDFs) to achieve the multiphysics coupling, and the 3D MHD-based arc model that satisfies the research demands in the present work is thus developed.

## 2.2. Structural Design of the PJT-GS and Electrode

An experimental prototype with a metal tank body is manufactured according to the experimental demands. The metal tank body is designed with a viewing window so that the variation of the arc morphology can be photographed using the high-speed camera. Moreover, the metal tank body is connected with a composite bushing on the top, and a pair of rotary electrodes is arranged in the central axis of the tank. The design of this metal tank body and the corresponding computation geometry in the present work is shown in Figure 2. The actual dimensions of the metal tank body are designed with a diameter of 750 mm and a height of 968 mm. Considering the performance requirements of the developed PJT-GS, the rotary electrode design is proposed, and the corresponding material is a 20% copper–80% tungsten alloy since it has relatively excellent resistance to erosion that results from the attachment of the hot arc column, as shown in Figure 3.

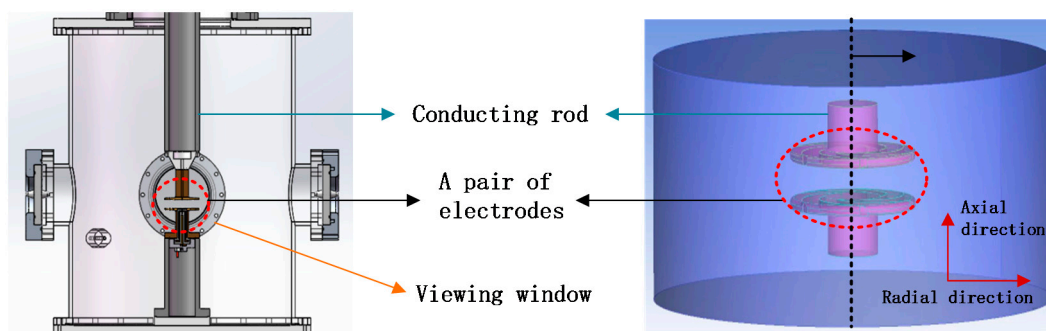


**Figure 2.** Structural design of the metal tank body of the PJT-GS prototype and the computational domain.

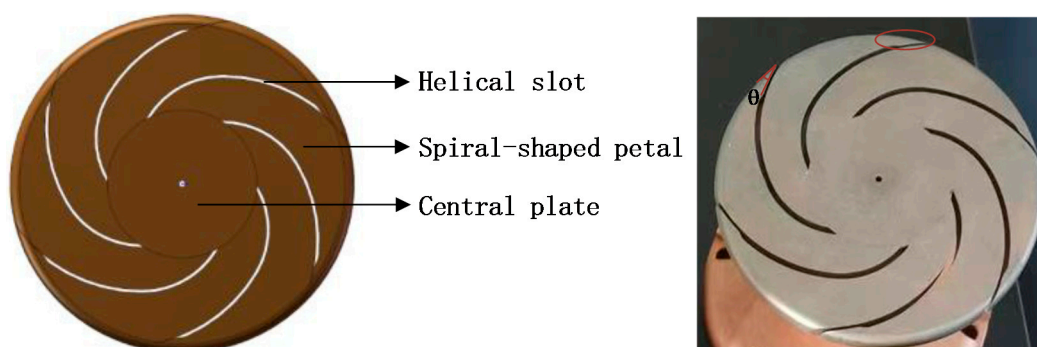


**Figure 3.** Structural design of the rotary electrode in the developed experimental PJT-GS prototype (Left) and the corresponding prototype of the electrode (right).

Actually, it should be pointed out that the unstructured grid system is used for the calculation of the present work. As presented in Figure 3, the diameter of the central plate is 48 mm, and the overall diameter of the electrode is 110 mm. However, the width of the helical slot is only 1 mm, and there is a narrow gap near the edge of the electrode that the width is even smaller, and the corresponding curvature is larger. The differential equations given in the form of Equation (1) cannot be directly solved by a computer. They need to be discretized into algebraic equations based on the chosen grid system. One of the main factors affecting the accuracy of the numerical calculations is the quality of the mesh. Mesh dissection of a regular hexahedron is not difficult whether using finite differences, finite elements or finite volumes. However, for a complex 3D structure, especially for geometrical structures that include a large number of curved surfaces, a large number of irregular mesh cells such as the unstructured grid is recommended, and the numbers of the cells for the whole computational domain are changed adaptively. The grid distribution is relatively dense in the arc-sensitive region and sparse at locations away from the arc.

It should also be mentioned that a 3D calculation is much more complicated than that of the 2D case, which is not only reflected in the equations to be solved, but the numbers of grid nodes and cells would be significantly increased as well. Nevertheless, the calculation efficiency would be largely limited, although the accuracy is ensured. Therefore, a sensitivity analysis is then performed to determine the computational domain that could satisfy the calculation requirement. The geometry is simplified such that it only keeps the two electrodes and conducting rods, and the computational domain is sensitively reduced to a diameter of 350 mm and a height of 170 mm, which is obtained from a comparison among different choices of the dimension, as shown in Figure 4. The axial and radial directions as shown in Figure 3 are respectively defined in a 2D plane. The temperature is chosen for evaluating the arc diffusion, of which the critical value is 3000 K. The reason that defines the boundary for the arc diffusion is to evaluate whether the surrounding solid object will be eroded by the hot arc or not. Actually, the used materials for the electrodes and tank of PJT-GS are respectively copper-tungsten alloy and aluminium alloy, of which

the boiling temperatures are respectively, 2835 K and 2740 K. Thus, 3000 K is reasonably determined to describe such a phenomenon.

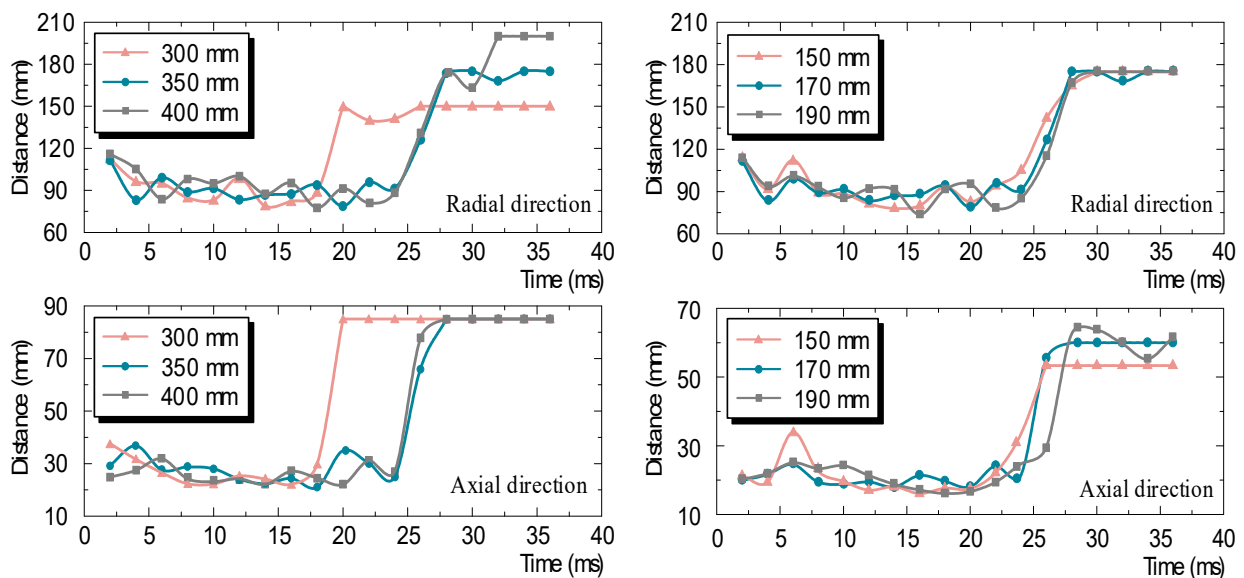


**Figure 4.** A comparison of the arc diffusion distances for different computational domains.

From the comparison, it is found that the choice of a smaller diameter of the computational domain leads to an earlier diffusion of the arc, while that obtained from the other two diameters presents a similar diffusion distribution, especially before 30 ms. The diffusion becomes larger for the choice of 400 mm after 30 ms. However, the current has already decreased to a lower value and the arc energy has also become lower so that the arc column would become thinner and shorter. Additionally, the high-temperature region around the boundary has mainly resulted from the diffusion of surrounding hot gas rather than the arc, so its effect on the arc dynamic behaviour can thus be neglected. Different heights of the computational domain also lead to a negligible effect on arc diffusion. It should be emphasised that a larger computational domain would also increase the total numbers of the grid cell, which limits the calculation efficiency. Therefore, a suitable computational domain is comparatively chosen to ensure both the calculation accuracy and efficiency.

### 2.3. Experimental Setup and Results

To verify the calculation results, a DC-based test circuit is constructed to support the current-flowing tests with a current up to 36 kA and a recovery voltage up to 160 kV, as shown in Figure 5 (left). A high-speed camera is arranged in front of the viewing window to photograph the movement of the arc. The arc current, the triggering voltage of the PJT-GS and the discharging voltage of the capacitor bank are respectively measured by a Rogowski coil and two high voltage probes and recorded by an oscilloscope. The typical waveforms of arc current and discharging voltage in the test are shown in Figure 5 (right). The operation frequency is 50 Hz. The framing speed of the camera is 1500 per second and the exposure time is 2  $\mu$ s. The components in the test circuit are explained in Table 3.

The arc morphology photographed from the current flowing test is shown in Figure 6. It is observed that the arc is initiated with a thinner column at the very beginning stage. With the transitory increase of the current during the first 2 ms, the arc column becomes thicker and rapidly moves to the right side of the electrode edge at 1.334 ms. Then the arc starts to move along the electrode edge with a clockwise rotation. The arc column is relatively short, and the arc is well controlled by the electrode during its rotation with a small diffusion roughly before 24 ms, and the corresponding current is still higher than 20 kA. After 24 ms, the arc current decreases at a faster rate and the generated electric energy becomes smaller. Then the arc starts to diffuse into its surroundings, and the arc column finally becomes smaller until its extinguishment. The arc totally rotates 18 turns

during the whole arcing process with an average rotation velocity of 179.4 m/s, and the average time duration for the rotation is 1.90 ms per circle (ms/pc).

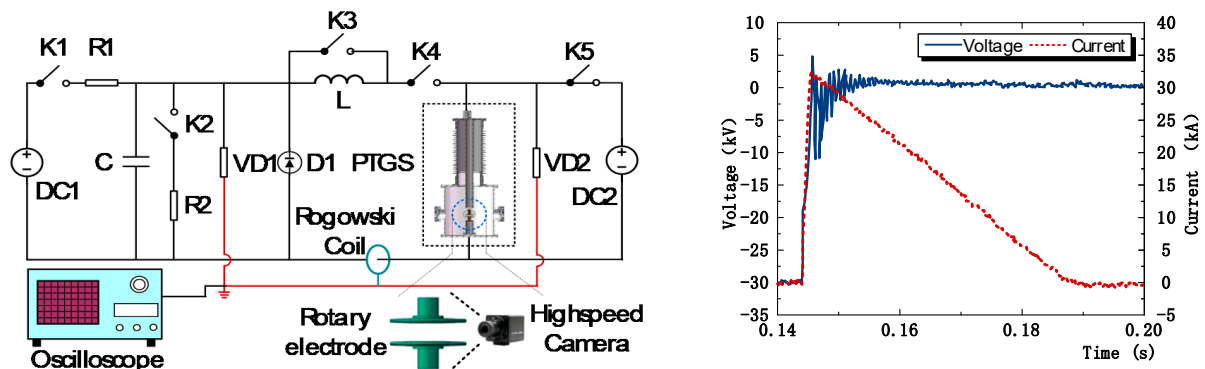


Figure 5. Schematic diagram of the test circuit with typical generated waveforms.

Table 3. Explanations of the components in the test circuit.

Symbols	Explanations	Symbols	Explanations
DC1	DC voltage source ( $V_{max} = 40$ kV)	L	Inductor (780 mH/1.6 mΩ)
K1	Charging switching	K3	Fast interrupter for protection
R1	Charging resistor (2400 W/60 kΩ)	D1	Freewheeling diode
C	Capacitor bank (1015 μF/36 kV)	K4	Vacuum circuit breaker
K2	Discharging switch	K5	Vacuum circuit breaker
R2	Discharging resistor (1 kΩ)	VD2	Resistor voltage divider
VD1	Resistor voltage divider	DC2	DC voltage source ( $V_{max} = 150$ kV)

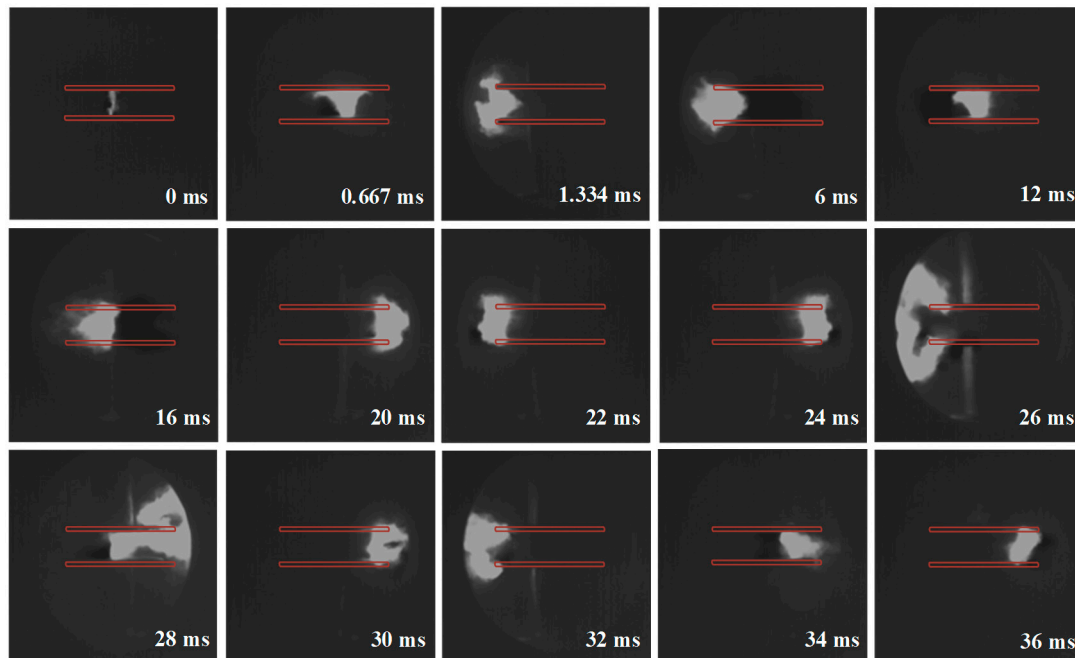


Figure 6. The arc morphology photographed during the 36 ms arcing process for a test case with a peak current of 33 kA.

Table 4 demonstrates the averaged rotation velocity of the arc for each turn during the whole arcing process. Actually, the averaged rotation velocity of the arc is determined by the circular path over the averaged rotation time. It is also found that the corresponding velocity, especially before 24 ms, is relatively faster than that of the later stage and it is because of the larger driving force (Lorentz force) generated by the flowed current. It could

thus be concluded that the current level is the decisive factor that would affect the rotational characteristics of the arc.

**Table 4.** Estimation of the averaged arc rotation velocity during the arcing process from experiment.

Turns	Momentary Current (kA)	Time Duration (ms/pc)	Average Velocity (m/s)	Turns	Momentary Current (kA)	Time Duration (ms/pc)	Average Velocity (m/s)
1st	31.30~29.37	2.33	148.3	10th	24.63~23.10	1.50	230.4
2nd	29.37~29.36	1.00	345.6	11th	23.10~22.70	2.00	172.8
3rd	29.36~28.89	1.67	206.9	12th	22.70~21.14	1.67	206.9
4th	28.89~27.41	1.00	345.6	13th	21.14~20.75	2.00	172.8
5th	27.41~26.63	1.33	259.8	14th	20.75~19.57	2.33	148.3
6th	26.63~26.62	1.33	259.8	15th	19.57~18.70	2.00	172.8
7th	26.62~26.20	1.33	259.8	16th	18.70~15.65	3.34	103.5
8th	26.20~24.67	1.67	206.9	17th	15.65~12.94	2.67	129.4
9th	24.67~24.63	1.67	206.9	18th	12.94~11.33	3.34	103.5

#### 2.4. Comparison between Calculation and Experiment

The calculated arc morphology with temperature distribution during the whole arcing process is shown in Figure 7. For such a calculation, an arc is initiated at the very beginning of the current-increasing period by placing a conducting hot column between the two electrodes. The temperature is defined to decrease gradually from the axis towards the radial direction. It should be emphasised that a condition of zero current density and magnetic vector potential is imposed on all boundary surfaces of the computation domain for the calculation of electric potential and magnetic flux density, which means that no current would have flowed across the boundary. Furthermore, the outer boundaries of the computational domain are sufficiently away from the arc region and the solutions of electric field and magnetic flux density inside the arc column and in its vicinity would not be affected by the use of the zero current density and zero magnetic vector potential at the boundary. Inside the chamber, the initial temperature of the cold gas is set to 300 K.

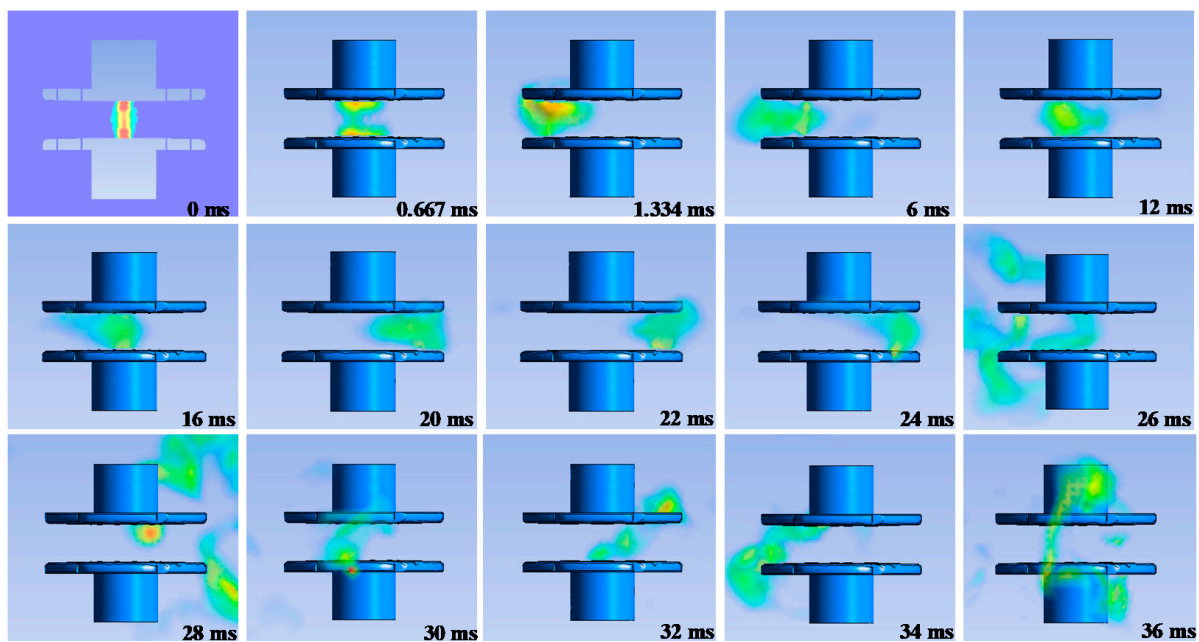


**Figure 7.** The arc morphology calculated using 3D arc model with a peak current of 33 kA.

From the calculation, it is found that the overall morphology of the arc shows a similar pattern in comparison with the experimental results. At the very beginning stage after the arc initiation, the arc column is limited to a small region and the surrounding cold gas

remains at a lower temperature. During arc rotation, the thermal energy generated by the current is mainly transferred to the surroundings through convection. The arc starts to diffuse, and the corresponding gas temperature becomes higher. With the comparison of the experiments, it is also found that the arc column moves behind the experiment result after 28 ms. It totally rotates 17 turns, and the average rotation time per circle is roughly 2.09 ms, which is 0.19 ms slower than that of the experiment.

Table 5 shows the averaged rotation velocity of the arc column for each turn during the arcing process as well, and the average velocity is roughly 7.7% slower than that obtained from the experiment. Actually, such a difference resulted from a simplification of the electrode geometry. It could be observed from Figure 3 that there exists a 0.1 mm narrow gap between the two spiral-shaped petals and the purpose of this design is to reduce the difficulty of arc moving across the petal. Nevertheless, the computation analysis becomes difficult due to the complicated geometrical structure. This smaller, narrower gap results in a denser distribution of the surrounding cells. The size is much smaller than 0.1 mm and it inevitably increases the total number of the grid cells in the computational domain, which significantly reduces the calculation efficiency. In addition, a smaller angle ( $\theta$ ) also causes a deterioration in the quality of surrounding grid cells, finally leading to poor convergence performance of the mathematical model. With a comprehensive consideration of calculation accuracy and efficiency, a chamfer is performed on the edge of the electrode, as shown in the red circular area of the right graph of Figure 3. This simplification leads to a slight increase in the distance between the spiral-shaped petals, and it is found from the calculation that the arc would be shortly stagnated when it travels across the gap. From the comparison between experiment and computation, it should be emphasised that the arc rotates approximately at a similar velocity during the high current phase ( $>20$  kA) and that the calculation error mainly occurs shortly before the arc quenching. The purpose of the present study is to explore the arc-controlling capability of the electrode in a comprehensive manner so as to optimise the operational performance of the PJT-GS. The exploration of such an arc controlling capability should pay more attention to the high current phase since the arc energy is much higher and the moving characteristics of the arc become more uncontrolled. A higher energy also has a stronger ablative effect on the surrounding solid objects, such as the conducting rod connected to the electrode plate and the inner wall of the sealed chamber of PJT-GS. During the low current phase, the arc rotation velocity would become slower due to the reduced driving force and the ablative effect would also be reduced due to the decrease in arc energy. The error obtained from this period could thus be reasonably neglected for comprehensively evaluating the corresponding arc controlling the performance of the electrode.

**Table 5.** Estimation of the averaged arc rotation velocity during the arcing process from calculation.

Turns	Time Duration (ms/pc)	Average Velocity (m/s)	Turns	Time Duration (ms/pc)	Average Velocity (m/s)
1st	2.2	157.1	10th	1.9	181.9
2nd	1.4	246.8	11th	1.6	216.0
3rd	1.6	216.0	12th	1.8	192.0
4th	1.5	230.4	13th	2.0	172.8
5th	1.4	246.8	14th	1.9	181.9
6th	1.4	246.8	15th	2.3	150.3
7th	1.4	246.8	16th	4.5	76.8
8th	1.5	230.4	17th	5.5	62.8
9th	1.6	216.0			

### 3. Analysis of the Variation of the Arc Dynamic Characteristics

#### 3.1. Effects of the Flowed Current Level

To comparatively study the effects of the current level flowing through the electrodes, a range of current is chosen to calculate the arc dynamic characteristics during its rotation. From Figure 8, it is observed that the arc under high current (>33 kA) behaves differently from the phenomenon of low current levels ( $\leq 20$  kA). The diffusion has fluctuated for the current below 20 kA, while it is relatively stable within a small region near the electrode edge for the current above 33 kA. The arc is diffused roughly within 90~100 mm from the center of the electrode, especially before 24 ms and it starts to diffuse to the computational boundary before the arc quenching, which implies that the diffusion of the arc seems more controllable with the increased current level, especially during the high currents of the whole arcing process. Such a phenomenon occurs both in axial and radial directions.

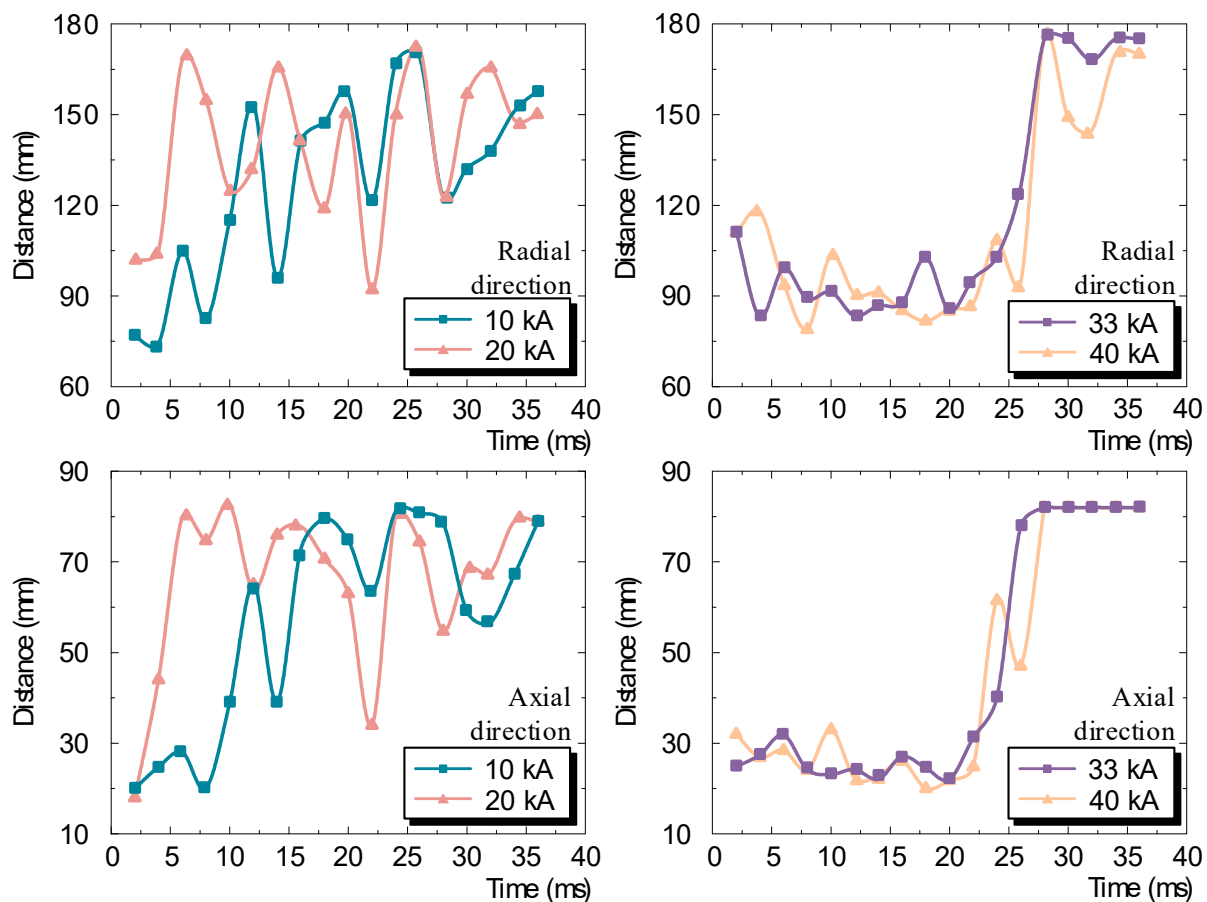


**Figure 8.** A comparison of arc diffusion under different current levels with a range between 10 kA and 40 kA.

The arc rotates 6.5 turns, 8 turns, 17 turns and 19.5 turns for the four cases from 10 kA to 40 kA, respectively. Furthermore, the rotation velocity of the arc also becomes faster with the increased current, as shown in Figure 9. The corresponding averaged velocity are 76.3 m/s, 86.9 m/s, 192.4 m/s and 206.7 m/s. Such increased velocity results from the difference in the driving force that triggers the arc column moving along the electrode edge. Actually, the current density is relatively higher at high current levels and the generated Lorentz force is correspondingly stronger, which could sufficiently constrict the arc under the impact of the self-induced magnetic field. Due to the action of the magnetic field during the arcing process, a constricted arc is developed and slowly accelerated towards the electrode edge at the very beginning stage. Since the arc rotation velocity for its first turn is comparatively slow, a higher current leads to a stronger diffusion. After the first turn, the arc formation tends to be established under the stronger action of the magnetic

field, so that the rotation velocity of the arc becomes larger. It could also be found that the rotation velocity of the arc is still below 150 m/s for the two cases of 10 kA and 20 kA while the velocity is higher than 150 m/s for most of the time during the arc rotation for the two cases of 33 kA and 40 kA, so that the arc could be well controlled within a small diffusion region. A lower velocity inevitably leads to insufficient energy exchange between the arc and the surrounding cold gas since the particles of the arc plasma would not sufficiently collide with the cold gas due to the lower velocity. However, a higher rotation velocity also indicates that the hot arc column would not be stagnated in one position on the electrode for a long time and the localized temperature on the electrode surface would not be excessively high. It could effectively reduce the erosion of electrode material caused by the presence of the hot arc column, and this is also the purpose of designing the rotary electrode with a helical-slot structure. The current flows from the conducting rod to the anode and continuously through the cathode to the cathode conducting rod. The relatively short route with small resistance could increase the current-carrying capability.

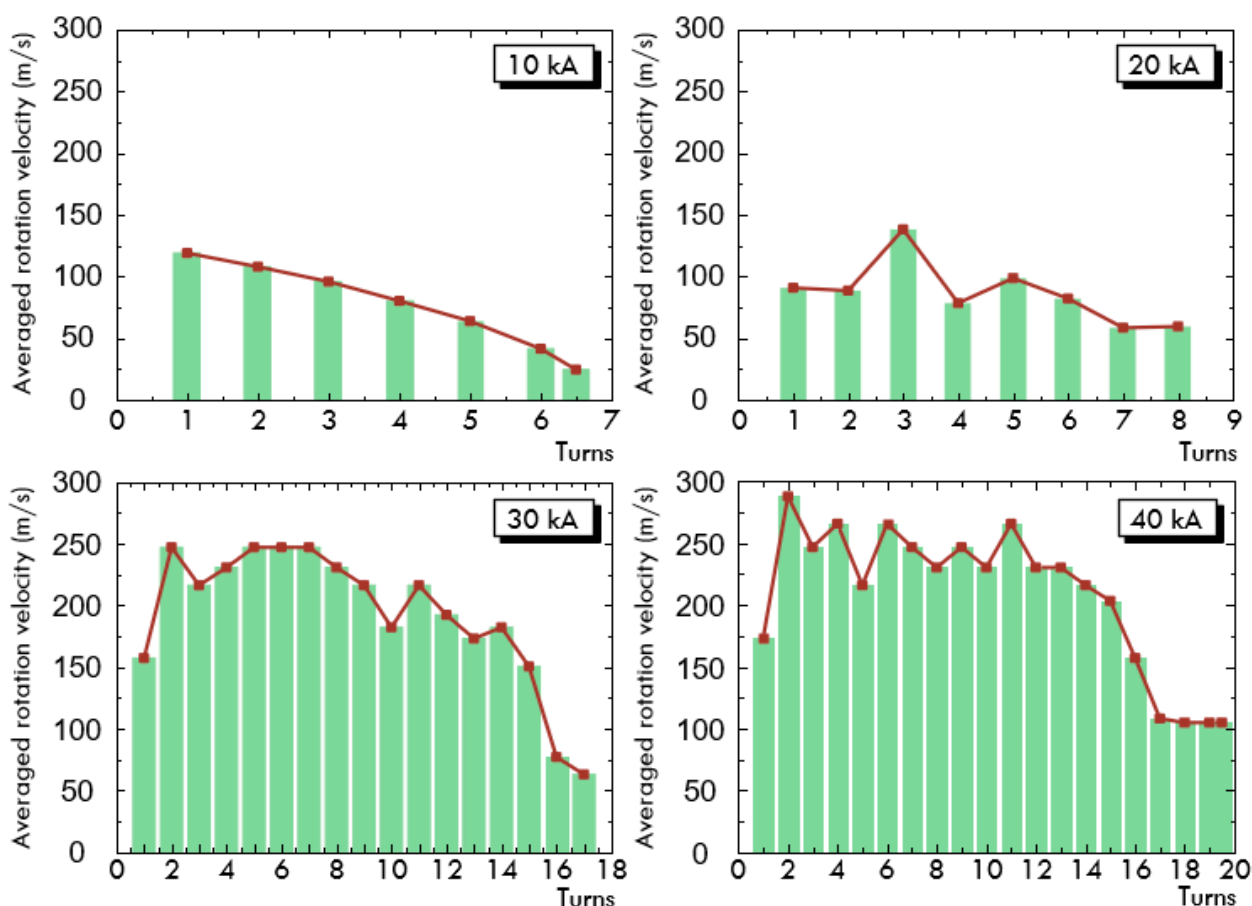


**Figure 9.** A comparison of the arc rotation velocity under different current levels with a range between 10 kA and 40 kA.

To comparatively study the varied distributions of the self-induced magnetic field as a result of the current level increase, the difference in magnetic flux density is then calculated using the 3D arc model and compared, as shown in Figure 10. Actually, the arc inevitably rotates across the spiral-shaped petals of the electrode due to the presence of the designed helical slots. The magnitude and direction of the magnetic flux density play a significant role during the arc rotation, especially through the helical slots. With a comparison of the B-field distribution at different time instants of the arcing process, it is observed that the magnetic flux density is largely distributed within the hot arc region and the corresponding value also becomes stronger with the increased current. When the current increases to its peak value, the maximum magnetic flux density increases from 0.198 T for the 10 kA case

to 0.770 T when the current increases to 40 kA. In addition, during the whole arc duration, the overall magnetic flux density becomes smaller as a result of the current decrease. By comparing the temperature distribution and the arc morphology at different time instants within the whole arc duration, as shown in Figure 7, it has been explained that the arc tends to be more stable at higher currents as a result of the relatively constricted shape of the arc column. However, the decreased current during the later stage of arc rotation leads to a lower level of the magnetic flux density, which means that the corresponding driven force to limit the arc rotation becomes smaller as well, so that the arc column excessively diffuses.

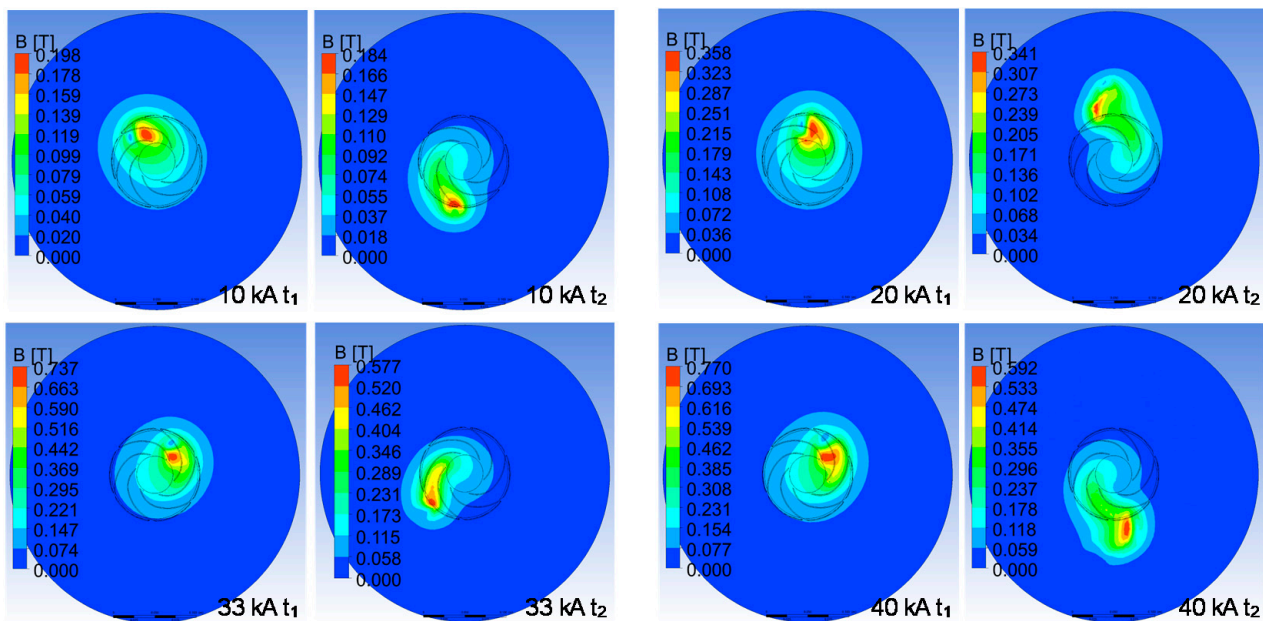


**Figure 10.** A comparison of the magnetic flux density under different current levels with a range between 10 kA and 40 kA.  $t_1$  and  $t_2$  respectively represents the time of peak current and 28  $\mu$ s.

The arc rotation velocity presents a similar pattern, as shown in Figure 11. The overall velocity of the arc column also decreases with the current within the whole arcing process, while the arc rotates faster when the flowed current level between the two electrodes becomes higher. Furthermore, the arc mostly rotates anticlockwise along the electrode edge and the flowing direction of the surrounding hot gas with a higher temperature is relatively concentrated. However, the velocity distributes more localized, especially for the case with a low current level (~10 kA). This is because the arc rotation velocity is highly related to the effects of the generated Lorentz force and the energy transfer process between the hot arc and its surroundings. For the 10 kA case, both the Lorentz force to control the arc rotation and the electrical power input to the arc are relatively lower, so that the arc only illustrates light diffusion outwards the boundary and the temperature of the surrounding cold gas remains lower due to insufficient energy exchange. With an increase in the flowed current, the Lorentz force and the arc energy both become larger, indicating that the arc becomes more capable of diffusing outwards. Therefore, it could reasonably be concluded that the TMF-based electrode design does have a strong current-carrying capacity and it also increases with the carrying current level. Besides that, the arc controlling performance of the TMF-based electrode gradually increases as well, especially within the high current phase in which the arc burns and rotates more steadily. Such a phenomenon also indirectly indicates that if the electrode itself is designed at a better arc controlling capability, then it would operate with a higher current carrying level.

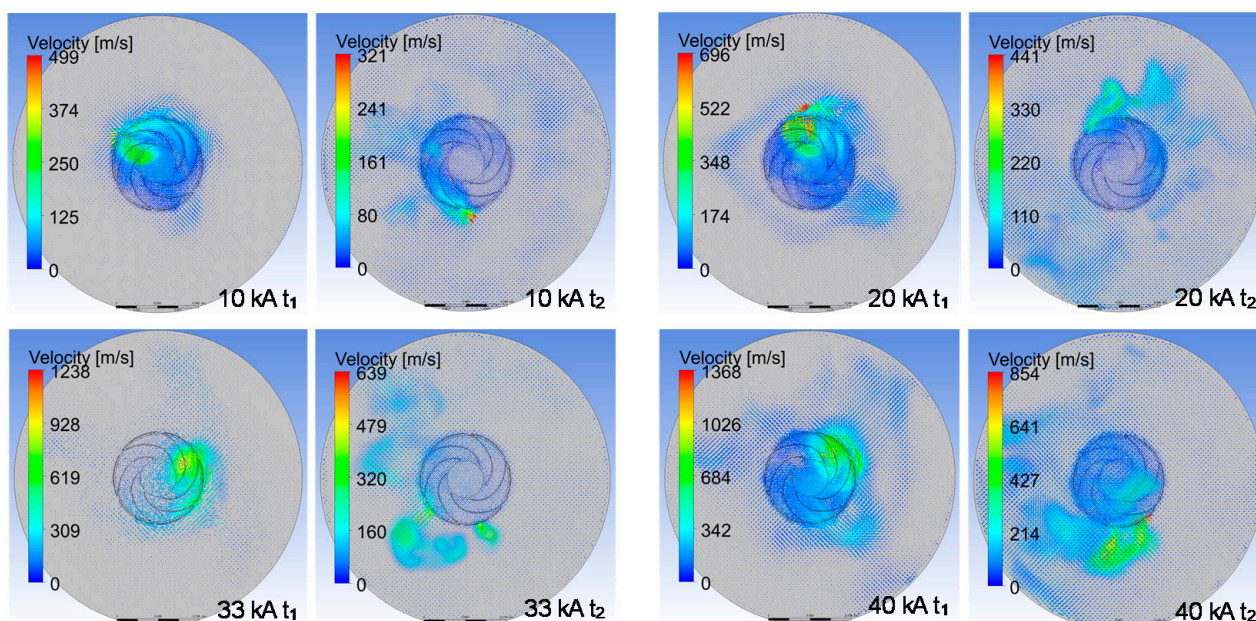


**Figure 11.** A comparison of the velocity vector under different current levels with a range between 10 kA and 40 kA.  $t_1$  and  $t_2$  respectively represents the time of peak current and 28  $\mu$ s.

### 3.2. Effects of the Gap Distance between Two Electrodes

In addition to the current level carried by the PJT-GS that would influence its operating performance, the gap distance between the two electrodes also sensitively affects the arcing characteristics. Figure 12 firstly shows the diffusion of the arc during the whole arcing process with different gap distances between the electrodes with a current of 33 kA, ranging from 5 mm to 30 mm. It is found that the arc rotates steadily during the high current phase when the gap distance is set below 10 mm. With a slight increase of the gap distance from 5 mm to 10 mm, the diffusion distance also demonstrates a minor increase, roughly from 65 mm to 70 mm in the radial direction and 10 mm to 15 mm in the axial direction, especially before 30 m/s. With the increase of the gap distance to 30 mm, the diffusion of the arc shows an overall increase as well, even higher than 80 mm in the radial direction and 20 mm in the axial direction. Besides that, the arc also becomes unstable during its rotation, which implies that the TMF-based electrode exhibits a better arc controlling performance at the short gap distance.

The variation of the arc dynamic characteristics under different gap distances could also be explained by the change of the B-field, as shown in Figure 13. With the increase of the gap distance from 5 mm to 30 mm, the value of the magnetic flux density presents an overall decrease. At the time instant when the current grows to its peak value, the maximum magnetic flux density is 0.796 T when the gap distance is set to 5 mm, while it drops to 0.574 T when the gap distance is increased to 30 mm. It indicates that the arc rotating performance is highly correlated with the B-field distribution, and it can be used as a performance evaluation parameter to estimate how strong the arc column could be driven to rotate circularly. In reality, the arc rotation velocity is mostly determined by the Lorentz force and the arc energy, as explained previously. The Lorentz force itself is dominantly determined by the interaction between the arc current and the self-induced magnetic field. From the calculations, it is also observed that the arc totally rotates 25 turns during the whole arcing process when the gap distance is set to 5 mm. The rotation velocity is comparatively faster with an averaged value of 245.4 m/s while it gradually decreases to 203.9 m/s, 171.8 m/s, 165.5 m/s and 127.6 m/s, respectively, for the cases with the gap distance increasing from 10 mm to 30 mm. The total turns for arc rotation are also correspondingly reduced from 25 to 20, 17.5, 17 and 13. Therefore, from the comparative analysis of the arc characteristics resulting from different gap distances, it could also be

reasonably pointed out that the arc controlling performance of the TMF-based electrode gradually decreases with an increase in the gap distance between the electrodes, and it also indicates that if the electrode itself is designed with better arc controlling capability, then it would operate with a better performance to withstand the operation condition with a larger gap distance.

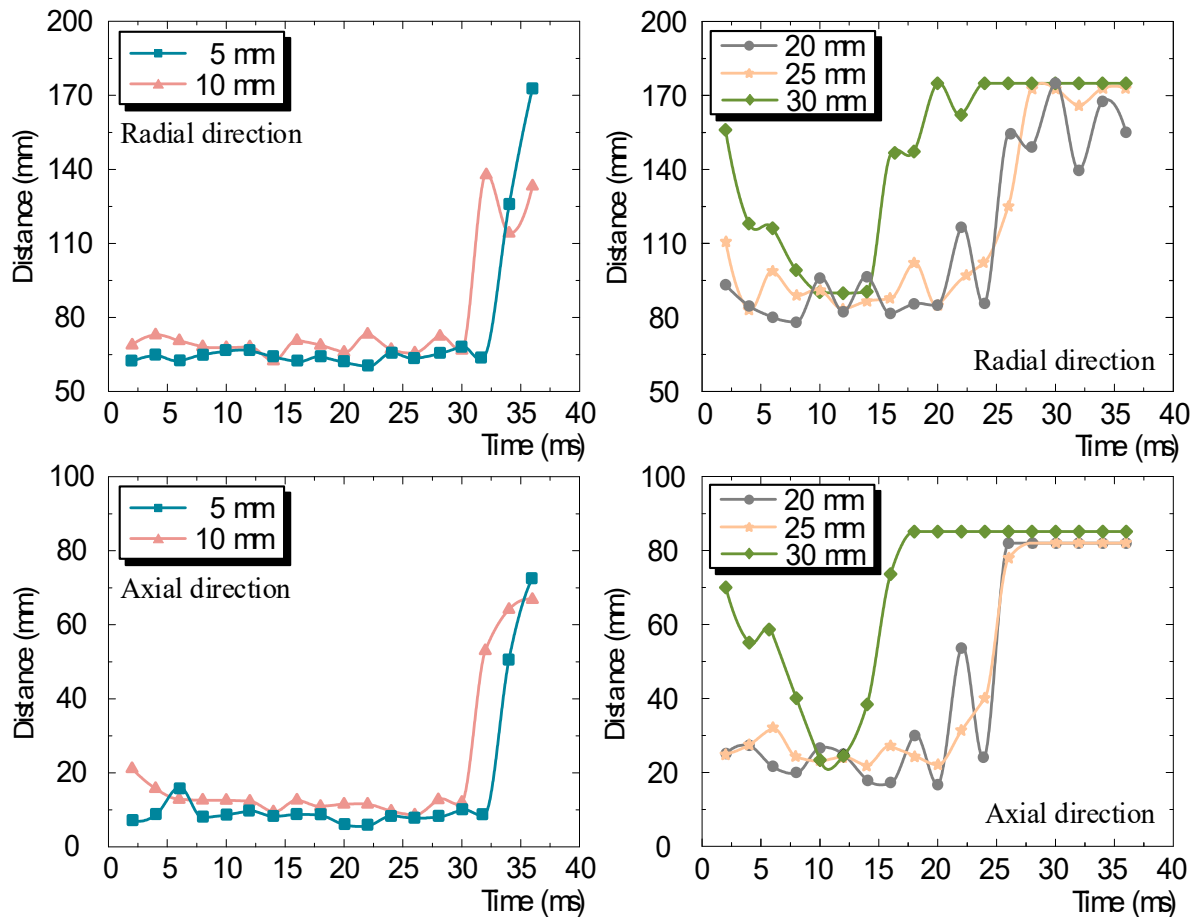


**Figure 12.** A comparison of arc diffusion under different gap distances between 5 mm and 30 mm.

From previous studies [33–35], it is observed that the faster the arc rotation velocity, the better it is controlled under the action of the electrode during the high current phase of an arcing process. From the present work, it is found that the velocity increase indicates a larger magnetic flux density, which also correspondingly implies that the designed electrode would be operated with a better arc controlling capability. Therefore, to substantiate those conclusions mentioned above, a comprehensive comparison of two electrodes with different arc controlling capabilities is also performed. The comparison was detailedly performed between the electrodes designed with different numbers of the spiral-shaped petal, including 6 and 8. From a comparison of the arc diffusion condition for these two designs of the electrode, it is found from Figure 14 that the electrode with 8 spiral-shaped petals has a better arc controlling capability during the whole arc duration since the average rotation velocity of the arc under the action of the electrode with 8 spiral-shaped petals is also faster, with a value of 196.8 m/s, which could sufficiently control the arc rotating steadily during the high current phase and gradually diffusing towards the computational edge, especially at the later stage.

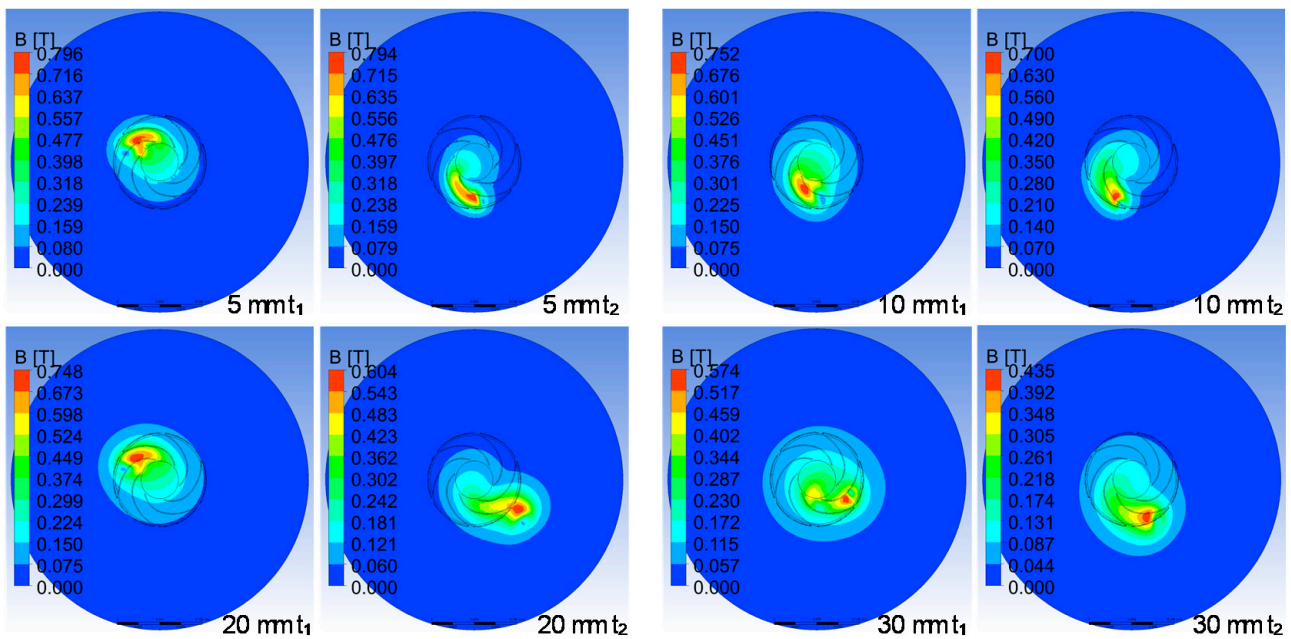


Figure 13. A comparison of magnetic flux density under different gap distances with a range between 5 mm and 30 mm.  $t_1$  and  $t_2$  respectively represents the time of peak current and  $28 \mu s$ .

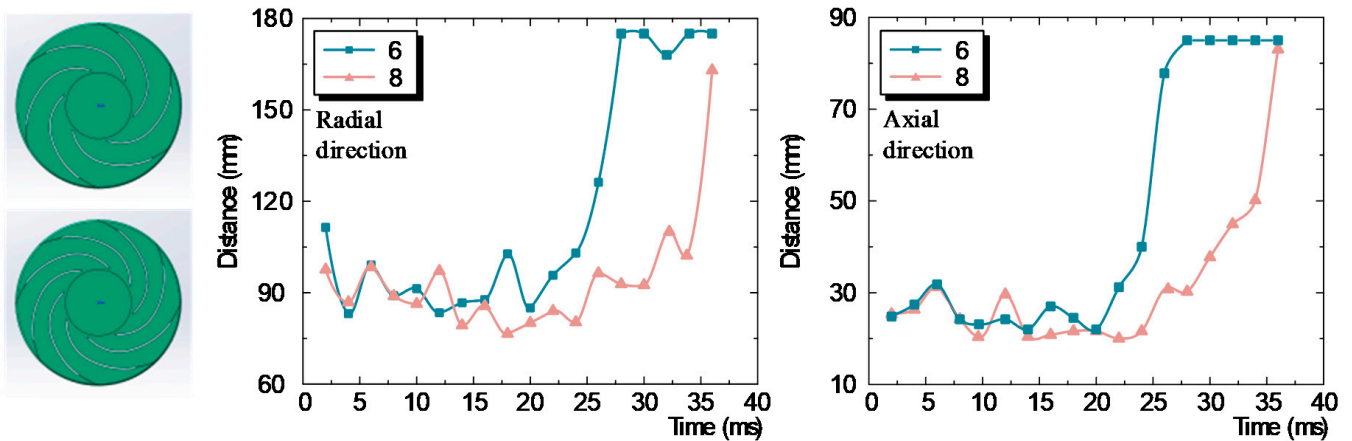


Figure 14. A comparison of arc diffusion under different electrode structure design with different numbers of the spiral-shaped petal.

Figures 15 and 16 present a detailed comparison of the arc diffusion conditions for the two electrode structure designs, both at different current levels and gap distances. From the comparison, it could be pointed out that the electrode structural design only presents a negligible effect on its arc controlling performance for the relatively lower current levels ( $<20 \text{ kA}$ ), and the arc still rotates unstably. However, in cases with high current levels, the increased arc-controlling performance of the electrode itself controls the arc to rotate within a smaller region, which is closer to the electrode edge. The diffusion of the arc when rotated at different gap distances shows a similar pattern, which implies that the electrode with better arc controlling performance has better adaptability to withstand the different operating conditions of the PJT-GS.

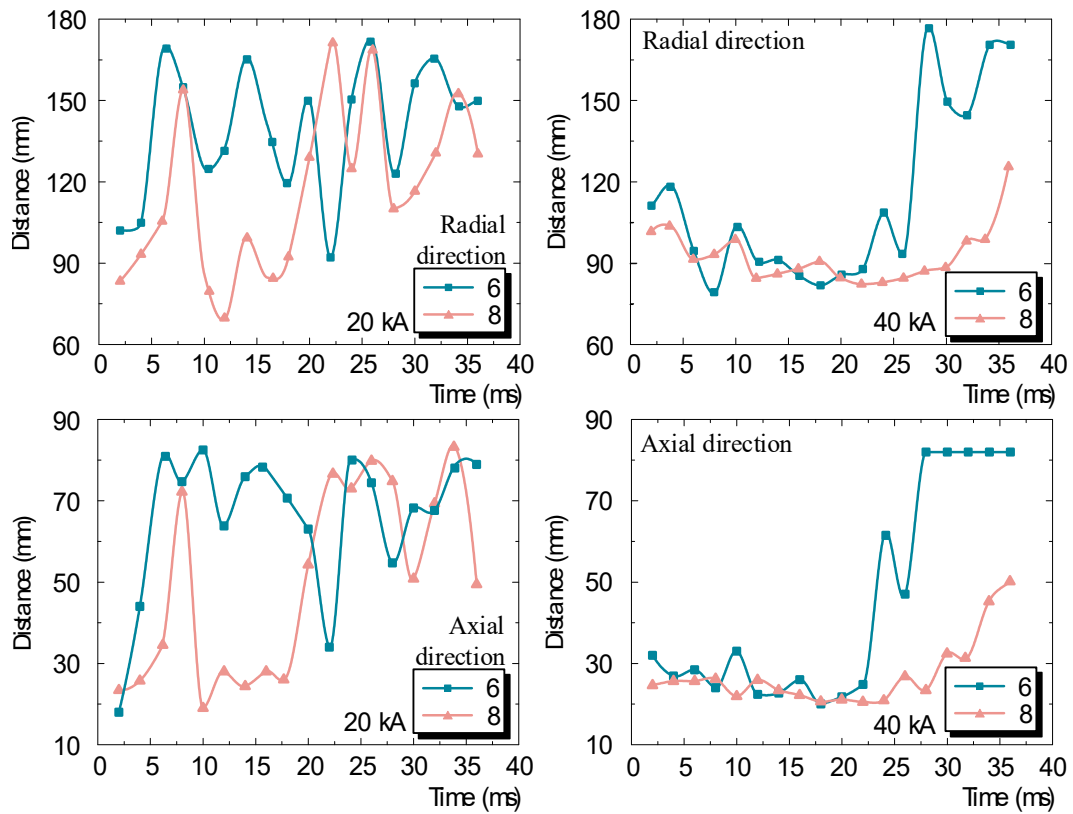


Figure 15. A comparison of arc diffusion under different electrode structure design with different numbers of the spiral-shaped petal at different current levels.

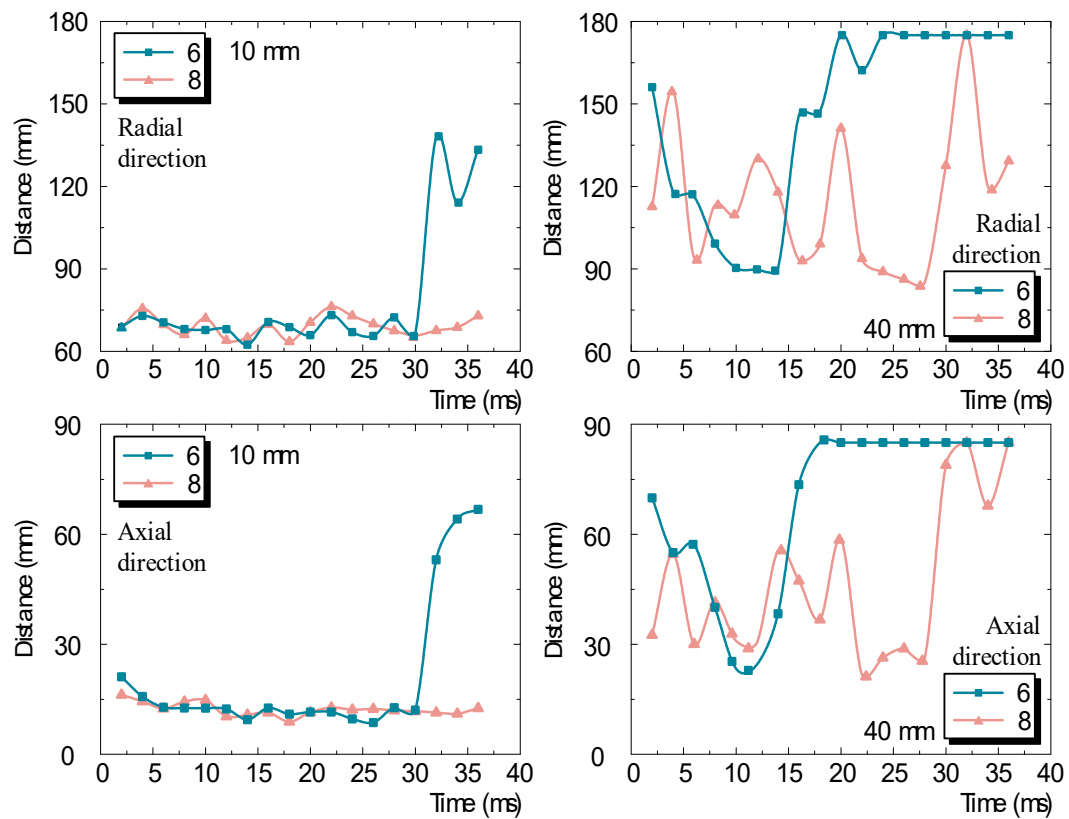


Figure 16. A comparison of arc diffusion under different electrode structure design with different numbers of the spiral-shaped petal at different gap distances.

#### 4. Conclusions

The arc dynamic characteristics driven by the TMF field during its rotation are comparatively studied in the present work to thoroughly analyse the variation of the arc performance when the PJT-GS operates under different conditions. From the research, the following conclusions could be summarized as follows:

- (1) In the present work, the computation results are comparatively studied by comparing them with the experimental results. The calculated arc morphology during its rotation within the whole 36 ms arc duration is firstly compared to the photographed results from the experiments, and it is found that the arc evolution process during the whole arc duration is comparable with the photographed results. The overall change in the velocity of the arc during its rotation and the change in velocity during each rotating turn are also compared. From the comparison, it could be found that the 3D arc model can reasonably describe the dynamic characteristics of the rotating arc. The calculated arc rotation velocity is also comparable with that obtained from the experiments, which indirectly proves the feasibility of the established mathematical model;
- (2) The diffusing and rotating characteristics of the arc during the arcing process are largely affected by the operation conditions of the PJT-GS as follows:
  - (i) With the increased current level that the PJT-GS withstands during its operation, the averaged rotation velocity of the arc also becomes speedier, respectively from 76.3 m/s to 86.9 m/s, 192.4 m/s and 206.7 m/s. With the increased rotation velocity, the arc is well controlled by the rotary electrode, and it could rotate within a smaller diffusion range at high currents;
  - (ii) With the increased gap distance between the two rotary electrodes inside the PJT-GS chamber, the averaged rotation velocity of the arc decreases from 245.4 m/s to 127.6 m/s and it is also largely diffused within the domain, which implies that the arc becomes increasingly difficult to control during its rotation;
- (3) The arc rotation velocity and the extent to which it diffuses outwards during the arcing process, especially in the high current phase, could reasonably provide a good assessment of the arc controlling performance presented by the designed electrode. The study of the dynamic characteristics of the arc under different conditions could effectively guide the design of the electrode and PJT-GS to achieve the improvement of their lifetime. This is because the better the arc is controlled, the less damage the electrode and the inner wall of the chamber will suffer. The erosion of the solid materials by the high-temperature arc would be reduced and the lifetime of the solid objects would be relatively improved to some extent.

**Author Contributions:** Conceptualization, W.W.; Data curation, X.Q.; Formal analysis, W.W.; Funding acquisition, Z.L.; Investigation, X.X.; Methodology, W.W.; Project administration, Z.L.; Software, X.Q.; Supervision, Z.L., K.G. and E.D.; Validation, K.G.; Writing—original draft, W.W. All authors have read and agreed to the published version of the manuscript.

**Funding:** This work was supported by Science and Technology Project of State Grid Corporation of China (5500-202155107A-0-0-00).

**Institutional Review Board Statement:** Not applicable.

**Informed Consent Statement:** Not applicable.

**Data Availability Statement:** Not applicable.

**Conflicts of Interest:** The authors declare no conflict of interest.

#### References

1. Li, Y.; Liu, J.; Xiao, H.; Zhang, Z.; Zhang, X.; He, M. A plasma-triggered gas switch. *Rev. Sci. Instrum.* **2018**, *89*, 094707. [[CrossRef](#)] [[PubMed](#)]
2. Hashemi, E.; Niayesh, K. DC current interruption based on vacuum arc impacted by ultra-fast transverse magnetic field. *Energies* **2020**, *13*, 4644. [[CrossRef](#)]

3. Wolf, C.; Kurrant, M.; Lindmayer, M.; Gentsch, D. Arcing behavior on different TMF contacts at high-current interrupting operations. *IEEE Trans. Plasma Sci.* **2011**, *39*, 1284–1290. [[CrossRef](#)]
4. Ma, H.; Zhang, Z.Q.; Geng, Y.S.; Wang, J.H.; Liu, Z.Y.; Yuan, F.X. Rotation characteristics of vacuum arcs drive by transverse magnetic fields. *IEEE Trans. Plasma Sci.* **2018**, *46*, 2181–2190. [[CrossRef](#)]
5. Wang, L.J.; Shi, W.X.; Lin, R.J.; Wang, Y.; Ma, J.W.; Jia, S.L. Experimental investigation of vacuum arc behavior under different contacts in vacuum interrupters. In Proceedings of the 2018 28th International Symposium on Discharges and Electrical Insulation in Vacuum (ISDEIV), Greifswald, Germany, 23–28 September 2018; pp. 223–226.
6. Delachaux, T.; Fritz, O.; Gentsch, D.; Schade, E.; Shmelev, D.L. Numerical simulation of a moving high-current vacuum arc driven by a transverse magnetic field (TMF). *IEEE Trans. Plasma Sci.* **2007**, *35*, 905–911. [[CrossRef](#)]
7. Zhu, L.Y.; Wu, J.W.; Zhang, X.M. Arc Movement of intermediate-frequency vacuum arc on TMF contacts. *IEEE Trans. Power Deliv.* **2013**, *28*, 2014–2021.
8. Liu, Z.Y.; Wang, Z.Y.; Zhang, X.; Wang, J.M. Analysis of axial magnetic field characteristics of coil type axial magnetic field vacuum interrupters. *Trans. China Electrotech. Soc.* **2007**, *22*, 47–53.
9. Duan, X.L.; Xiu, S.X.; Wu, S.F.; Feng, D.Y.; Ye, H.S.; Li, Q. Characteristic of wan-type transverse magnetic field contacts of vacuum circuit breaker. *High Volt. Appar.* **2017**, *53*, 57–63.
10. Xiu, S.X.; Pang, L.; Wang, J.M. A new electrode applied to high voltage vacuum interrupter and its performance. *Proc. CSEE* **2008**, *28*, 124–129.
11. Deng, J.; Wang, L.J.; Qin, K.; Zhang, X.; Jia, S.L.; Shi, Z.Q. Experimental and simulation of triggered vacuum arc under TMF-AMF contact. In Proceedings of the 2016 27th International Symposium on Discharges and Electrical Insulation in Vacuum (ISDEIV), Suzhou, China, 18–23 September 2016; pp. 1–4.
12. Lei, B.S.; Cheng, K.; Kong, C.C.; Yang, Z.M. Progress of magnetic contacts in vacuum interrupter. *Vac. Electron.* **2019**, *5*, 1–6.
13. Johnsen, S.G.; Simonsen, A. CFD modeling of a rotating arc plasma reactor. In Proceedings of the 10th International Conference on CFD in Oil & Gas, Metallurgical and Process Industries, Trondheim, Norway, 17–19 June 2014.
14. Kadivar, A.; Kaveh, N. Effects of fast elongation on switching arcs characteristics in fast air switches. *Energies* **2020**, *13*, 4846. [[CrossRef](#)]
15. Verite, J.C.; Boucher, T.; Comte, A.; Delalondre, C.; Simonin, O. Arc modelling in circuit breakers: Coupling between electromagnetics and fluid mechanics. *IEEE Trans. Magn.* **1995**, *31*, 1843–1848. [[CrossRef](#)]
16. Versteeg, H.K.; Malalasekera, W. *An Introduction to Computational Fluid Dynamics: The Finite Volume Method*, 2nd ed.; Prentice Hall: Hoboken, NJ, USA, 2007; Volume 520, pp. 9–38.
17. Shercliff, J.A. *Magnetohydrodynamics*; Pergamon Press: Oxford, UK, 1965.
18. Alberghi, C.; Candido, L.; Testoni, R.; Utili, M.; Zucchetti, M. Verification and validation of COMSOL magnetohydrodynamic models for liquid metal breeding blankets technologies. *Energies* **2021**, *14*, 5413. [[CrossRef](#)]
19. Wang, G.; Wang, Y.; Zhang, L.; Xue, S.; Dong, E.; Zou, J. A novel model of electromechanical contactors for predicting dynamic characteristics. *Energies* **2021**, *14*, 7466. [[CrossRef](#)]
20. Yan, J.D.; Fang, M.T.C.; Hall, W. The development of PC based CAD tools for auto-expansion circuit breaker design. *IEEE Trans. Power Deliv.* **1999**, *14*, 176–181. [[CrossRef](#)]
21. Tang, K.M.; Yan, J.D.; Chapman, C.; Fang, M.T.C. Three-dimensional modelling of a dc arc plasma in a twin-torch system. *J. Phys. D.* **2010**, *43*, 345201. [[CrossRef](#)]
22. Wu, Y.; Rong, M.Z.; Yang, Q.; Hu, G.X. Simulation on dynamic characteristics of arc in low voltage circuit breaker modelling. *Proc. CSEE* **2005**, *25*, 143–148.
23. Blais, A.; Proulx, P.; Boulos, M. Three-dimensional numerical modelling of a magnetically deflected dc transferred arc in argon. *J. Phys. D.* **2003**, *36*, 488. [[CrossRef](#)]
24. Phanoraj, V.; Phadke, A.G. Modelling of circuit breakers in the electromagnetic transients program. *Physics* **1988**, *3*, 799–805. [[CrossRef](#)]
25. Hsu, K.C.; Ptender, E. Analysis of the cathode region of a free-burning high intensity argon arc. *J. Phys. D* **1983**, *54*, 3818–3824. [[CrossRef](#)]
26. Trelles, J.P. Nonequilibrium Phenomena in (Quasi-)thermal Plasma Flows. *Plasma Chem. Plasma Process.* **2020**, *40*, 727–748. [[CrossRef](#)]
27. Mohsni, C.; Baeva, M.; Franke, S.; Gortschakow, S.; Araoud, Z.; Charrada, K. Effect of a bidirectional coupling of an LTE arc column to a refractory cathode in atmospheric pressure argon. *Phys. Plasmas* **2020**, *27*, 073514. [[CrossRef](#)]
28. Baeva, M.; Benilov, M.S.; Almeida, N.A.; Uhrlandt, D. Novel non-equilibrium modelling of a DC electric arc in argon. *J. Phys. D Appl. Phys.* **2016**, *49*, 245205. [[CrossRef](#)]
29. Bhigamudre, V.G.; Trelles, J.P. Characterization of the arc in crossflow using a two-temperature nonequilibrium plasma flow model. *J. Phys. D Appl. Phys.* **2018**, *52*, 015205. [[CrossRef](#)]
30. Saifutdinov, A.I. Unified simulation of different modes in atmospheric pressure DC discharges in nitrogen. *J. Appl. Phys.* **2021**, *129*, 093302. [[CrossRef](#)]
31. Pei, Y.Q.; Zhong, J.Y.; Zhang, J.M.; Yan, J.D. A comparative study of arc behaviour in an auto-expansion circuit breaker with different arc durations. *J. Phys. D Appl. Phys.* **2014**, *47*, 335201. [[CrossRef](#)]

32. Xi'an Jiaotong University: Gas Discharge Plasma Database. Available online: <https://plasma-data.net/index> (accessed on October 2021).
33. Guo, R.; He, J.J.; Zhao, C.; Chen, L.X.; Pan, Y. A Rotating Arc Gap Switch and its Arc Velocity Characteristics. *Proc. CSEE* **2011**, *31*, 125–129. [[CrossRef](#)]
34. He, J.J.; Guo, R. Measurement of arc velocity in a rotating arc pulsed power switch based on B-dot probes. *IEEE Trans. Plasma Sci.* **2010**, *38*, 2669–2674. [[CrossRef](#)]
35. Dullni, E. Motion of high-current vacuum arcs on spiral-type contacts. *IEEE Trans. Plasma Sci.* **1989**, *17*, 875–879. [[CrossRef](#)]